Supplementary Information

Ultrathin aluminum–air batteries via hygroscopic electrolytes for continuous operation of imperceptible on-skin electronics

Jaeil Park[1], Inho Lee[2], Namhee Kim[1], Wonseok Shin[1], Joo Sung Kim[3], Daegun Kim[4], Giwon Lee[5], Jinhan Cho[6], Hoon-Hee Ryu[7], Myung-Han Yoon[8], Seung Joon Yoo[8]*, Woo-Jin Song[7,9]** and Sungjun Park[1,2]***

[1]Department of Electrical and Computer Engineering, Ajou University, Suwon 16499, Republic of Korea
[2]Department of Intelligence Semiconductor Engineering, Ajou University, Suwon 16499, Republic of Korea
[3]Thin-Film Device Laboratory, RIKEN, Wako, Saitama 351-0198, Japan
[4]School of Chemical, Biological, and Battery Engineering, Gachon University, Seongnam 13120, Republic of Korea
[5]Department of Chemical Engineering, Kwangwoon University, Seoul 01897, Republic of Korea
[6]School of Chemical and Biomolecular Engineering, Korea University, Seoul 02841, Republic of Korea
[7]Department of Chemical Engineering and Applied Chemistry, Chungnam National University, Daejeon 34134, Republic of Korea
[8]Department of Materials Science and Engineering, Gwangju Institute of Science and Technology, Gwangju 61005, Republic of Korea
[9]Institute of Carbon Fusion Technology (InCFT), Chungnam National University, Daejeon, 34134, Republic of Korea

*Correspondences: sjoonyoo@gist.ac.kr
**Correspondences: wjsong@cnu.ac.kr
***Correspondences: sj0223park@ajou.ac.kr

Keywords: On-skin batteries, hygroscopic hydrogel electrolytes, self-hydration, aluminum-corrosion suppression, skin-conformal biosensors

Table of contents

Supplementary experiment sections

Fabrication of skin-conformal substrates for biosensor system

Glass substrates were sequentially cleaned with detergent, deionized water, acetone, and isopropyl alcohol for 5 min each under ultrasonic agitation. To enable facile delamination, a fluorinated polymer solution (Novec 1700:7100, 1:10 vol%, 3M™) was spin-coated onto the glass surface at 2000 rpm for 60 s to form a release layer. A 1 μm-thick parylene C (PaC) film was subsequently deposited on top via chemical vapor deposition and annealed at 120 ℃ for 1 h. To planarize the PaC surface, a 500 nm-thick epoxy layer (SU-8 3005, MicroChem) was spin-coated at 5000 rpm for 60 s and prebaked at 95 °C for 2 min. The film was then exposed to UV light for 4 min, baked again at 95 °C for 3 min, and finally annealed at 120 °C for 1 h to complete substrate preparation.

Fabrication of ultrathin organic electrochemical transistors for physiological signal sensor

Ultraflexible organic electrochemical transistors (OECTs) were fabricated on prefabricated ultrathin skin-conformal substrates. The drain and source electrodes (Cr/Au, 5/45 nm) were defined by standard photolithography followed by thermal evaporation and lift-off. For the active channel, a solution comprising poly(3,4-ethylenedioxythiophene):polystyrene sulfonate (PEDOT:PSS, 2 mL; Clevios PH1000, Heraeus), ethylene glycol (0.1 mL; Sigma-Aldrich), and dodecylbenzene sulfonic acid (5 μL; Sigma-Aldrich) was spin-coated onto the electrode-patterned substrate at 1,500 rpm for 60 s. The coated film was subsequently annealed at 120 °C for 1 h to enhance the conductivity through cross-linking of the PEDOT:PSS network.

The active layer was then patterned using conventional photolithography and dry etching to define the transistor channel. For passivation, an SU-8 layer (MicroChem) was spin-coated at 3,000 rpm for 40 s, prebaked at 90 °C for 2 min, and exposed to UV light for 48 s through a chrome photomask using a mask aligner (MDA-400S, MIDAS System). The exposed film was post-baked at 90 °C for 2 min and developed in SU-8 developer (MicroChem) for 2 min to complete the encapsulation process.

OECT characterization and analysis

Electrical characterization of the OECTs was carried out under ambient conditions using two source-measure units (Keithley 2400). All measurements were performed in phosphate-buffered saline (PBS) electrolyte, with an Ag/AgCl electrode immersed in a KCl solution serving as the gate terminal. Device operation and data acquisition were controlled through custom LabVIEW scripts.

Supplementary Figures

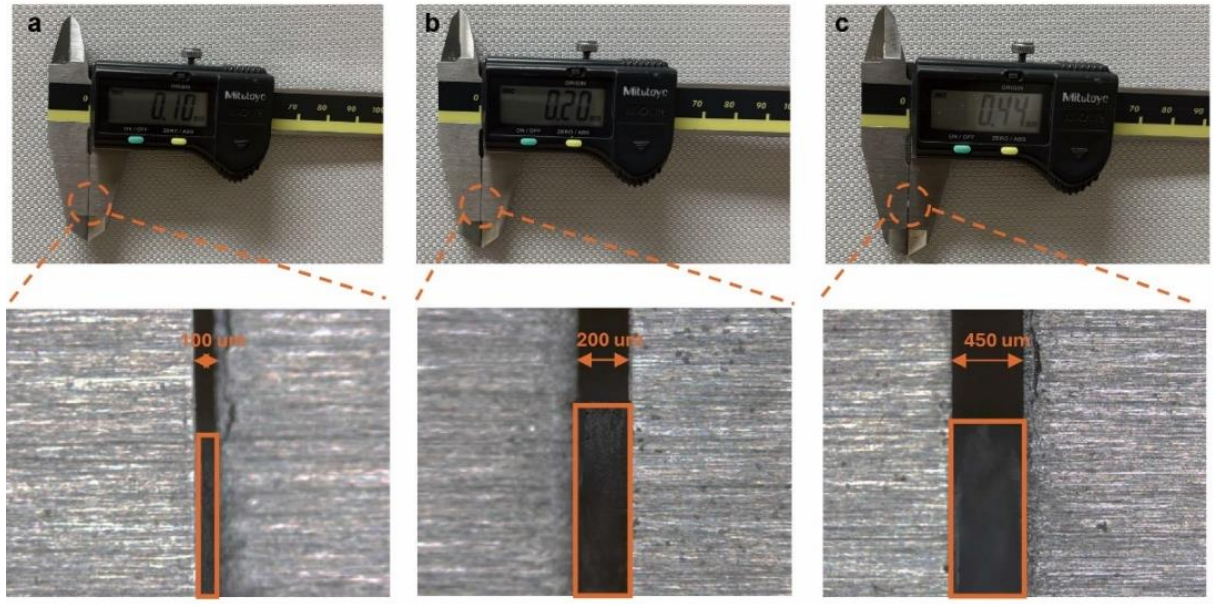

Fig. S1 Photographs of HHEs with thicknesses of **a,** 100 μm, **b,** 200 μm, and **c,** 450 μm. The reported HHE thicknesses were measured in the as-prepared hydrated state before additional ambient moisture uptake. This controllable thickness is a key structural advantage for ultrathin on-skin AABs, because reducing the electrolyte thickness lowers the overall device profile.

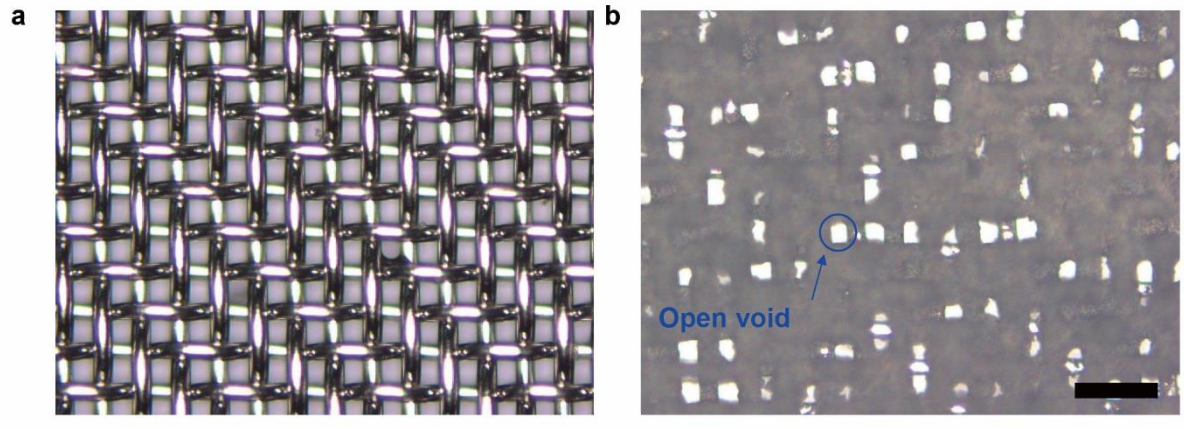

Fig. S2 Optical images of the plain-woven stainless-steel mesh used as the gas diffusion layer **a,** before and **b,** after Pt/C catalyst coating. The diameter of an individual wire is 25 μm. Scale bar denotes 100 μm. The plain-woven stainless-steel mesh is a structurally advantageous gas-diffusion layer for ultrathin H-AABs. Even after Pt/C coating, open voids remain clearly observable in the mesh structure, indicating that the porous framework is preserved and can still provide pathways for air transport while accommodating catalytic sites. Furthermore, the breathable woven architecture offers mechanical compliance under deformation, which is beneficial for maintaining electrochemical functionality in flexible and on-skin battery configurations.

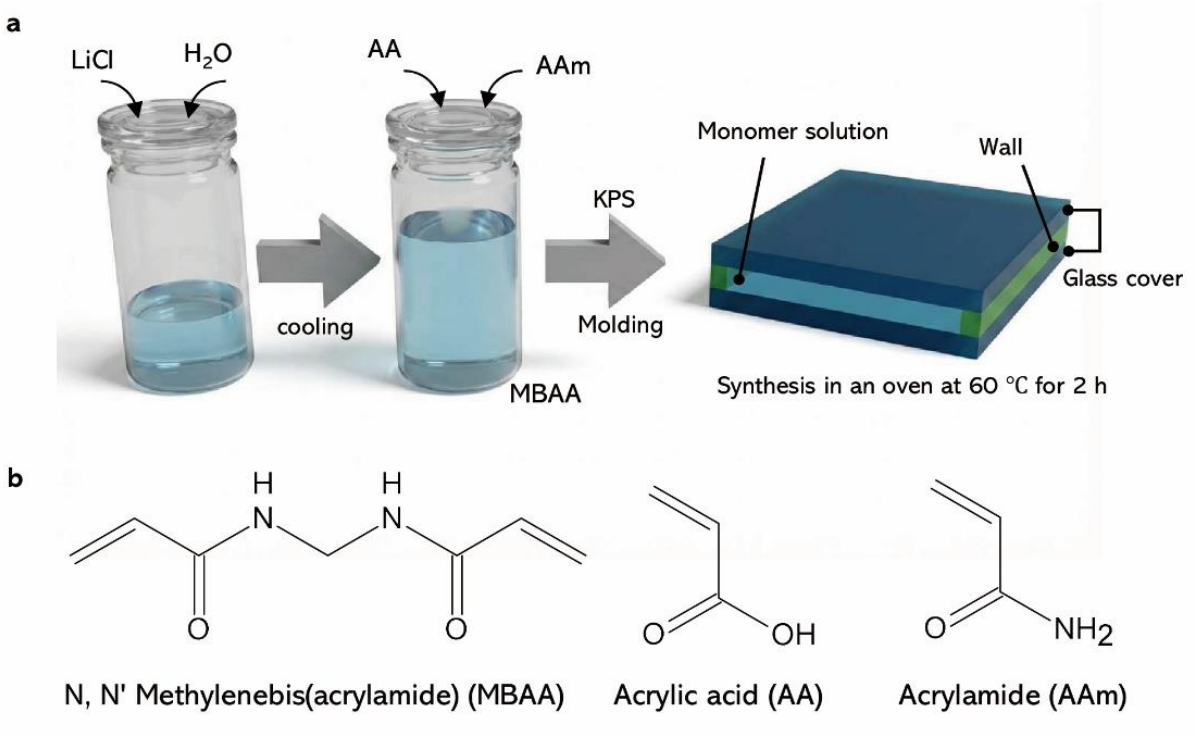

Fig. S3 a, Schematic illustration of the synthesis procedure for Poly(AA-r-AAm) copolymer-based hygroscopic hydrogel electrolytes. **b,** Chemical structures of AA, AAm, and MBAA used to form the HHE matrix. The HHEs were constructed from a crosslinked Poly(AA-r-AAm) copolymer network, in which acrylic acid and acrylamide provide abundant hydrophilic functional groups for interacting with water molecules and dissolved ions. In addition, the incorporation of MBAA as a crosslinker enables formation of a three-dimensional polymer framework, which helps maintain structural integrity even in ultrathin configurations. Such a chemically functional and mechanically stable network provides a suitable matrix for salt incorporation, moisture uptake, and ion transport, thereby supporting the self-hydrating and electrolyte-retaining characteristics of the HHEs.

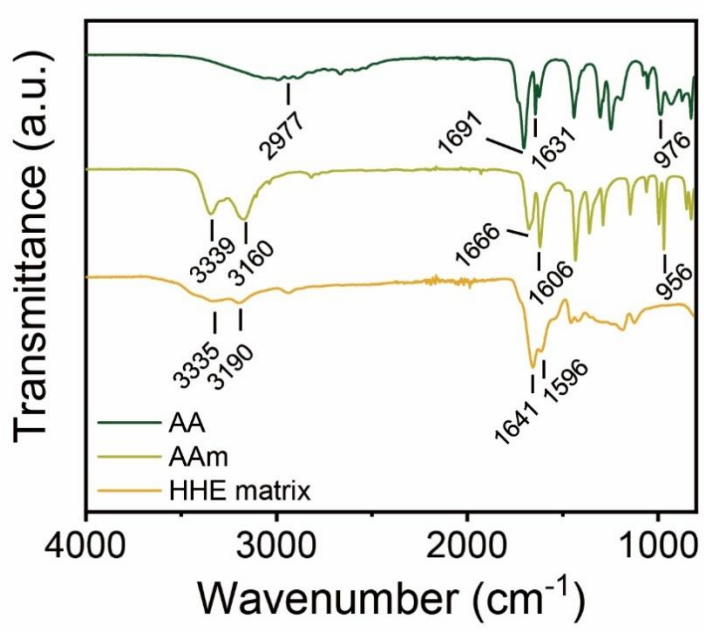

Fig. S4 FT-IR spectra of acrylic acid (AA), acrylamide (AAm), and the synthesized Poly(AA-r-AAm) HHE matrix. The acrylic acid (AA) spectrum exhibited a broad OH stretching band of the carboxylic acid group around 2,977 cm^{-1}, together with characteristic peaks at 1,691 cm^{-1} (C=O), 1,631 cm^{-1} (C=C), and 976 cm^{-1} (C=C–H), confirming the presence of the vinyl and carboxylic acid functionalities in the monomer. The acrylamide (AAm) spectrum showed characteristic NH stretching bands of the amide group at 3,339 and 3,160 cm^{-1}, along with peaks at 1,666 and 1,606 cm^{-1}, which are attributed to amide-related vibrations and NH bending modes. Although the C=C stretching peak was not clearly distinguishable in the AAm spectrum, the C=C–H peak at 956 cm^{-1} was clearly observed, indicating the presence of the vinyl group in the monomer. In contrast, the synthesized hydrogel matrix exhibited spectral features closer to those of AAm because of the AA:AAm feed ratio of 1:3. Notably, the vinyl-related C=C–H peak in the 1000–950 cm^{-1} region disappeared after polymerization, confirming that the C=C double bonds of the monomers were consumed during polymerization. These results support the successful copolymerization of AA and AAm into the hydrogel matrix.

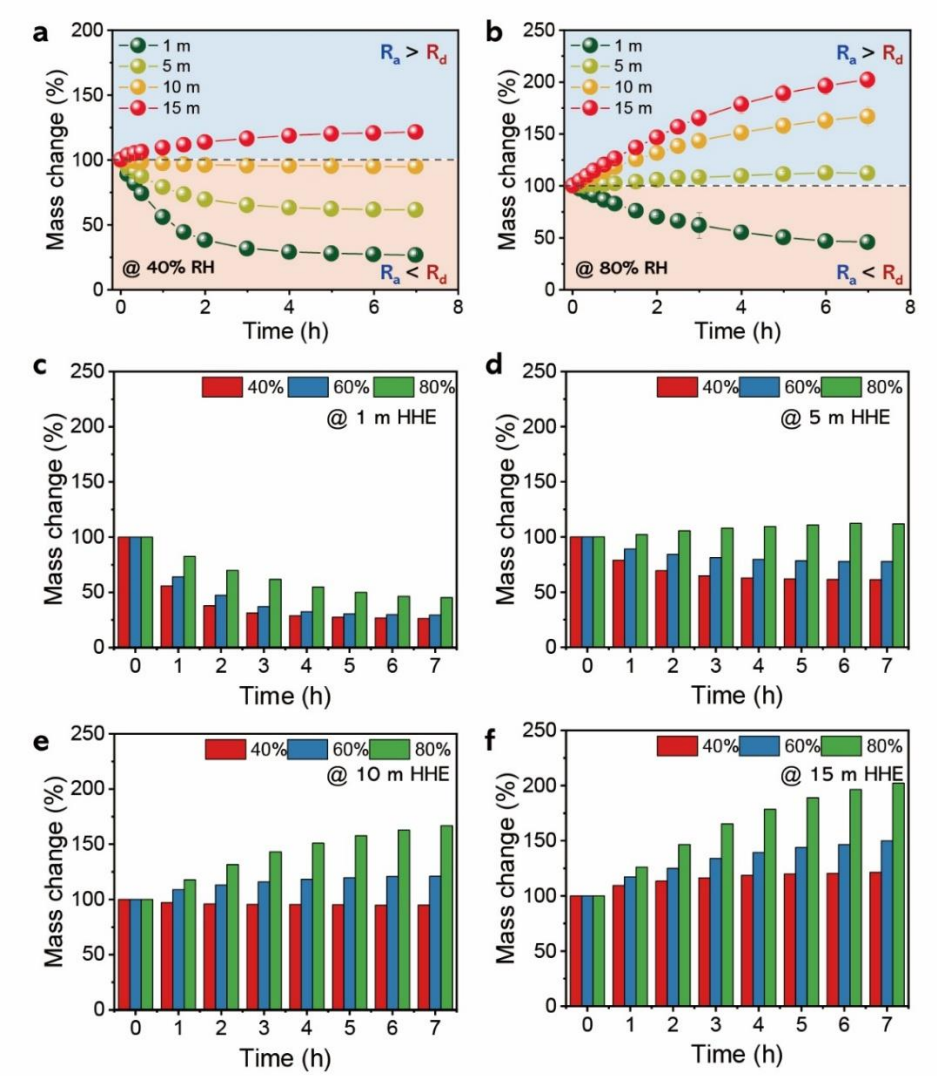

Fig. S5 Time-dependent mass change profiles of the as-prepared HHEs under air at **a,** 40% RH and **b,** 80% RH. **c–f)** Bar graphs summarizing the mass changes of **c,** 1 m, **d,** 5 m, **e,** 10 m, and **f,** 15 m HHEs after 7 h under air at different RH. The 1 m HHEs, which exhibit weak hygroscopicity, showed a marked decrease in mass to 26.3%, 29.5%, and 45.3% of their initial mass after 7 h under 40%, 60%, and 80% RH, respectively. In contrast, the 15 m HHEs, which exhibit strong hygroscopicity, showed a rapid increase in mass to 121.3%, 150.0%, and 202.1% of their initial mass after 7 h under 40%, 60%, and 80% RH, respectively. These results confirm that highly concentrated HHEs can maintain or even replenish their water content under ambient conditions, which is particularly advantageous for ultrathin electrolyte systems with limited initial water reservoirs.

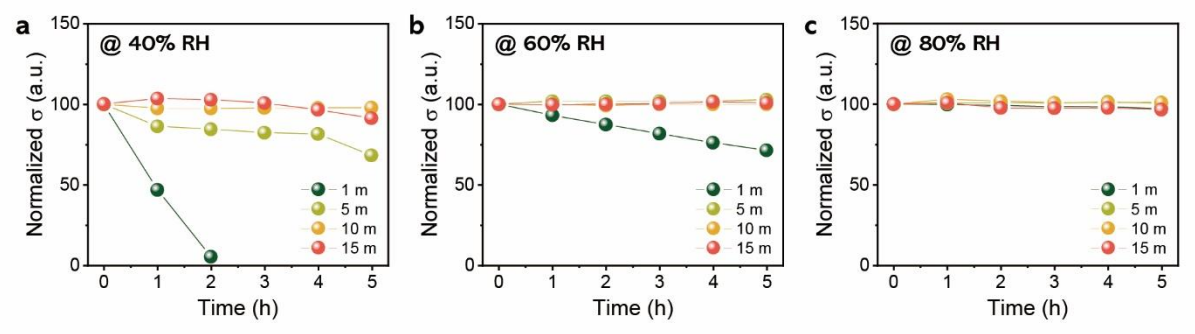

Fig. S6 Normalized ionic conductivity of the as-prepared HHEs under air at **a,** 40% RH, **b,** 60% RH and **c,** 80% RH. The normalized ionic conductivity of the 1 m HHE steeply decreased over time under air at 40% RH, whereas those of the highly concentrated HHEs remained nearly unchanged. At higher RH values of 60% and 80%, only the 1 m HHE exhibited a slight decrease, while no significant change was observed for the other concentrations. This concentration-dependent behavior indicates that low-concentration HHEs are vulnerable to dehydration-induced degradation of ionic transport, while highly concentrated HHEs can preserve stable ion-conduction pathways under various RH conditions. Such stability is particularly important for ultrathin electrolyte systems, where maintaining ionic conductivity is essential for sustained battery operation.

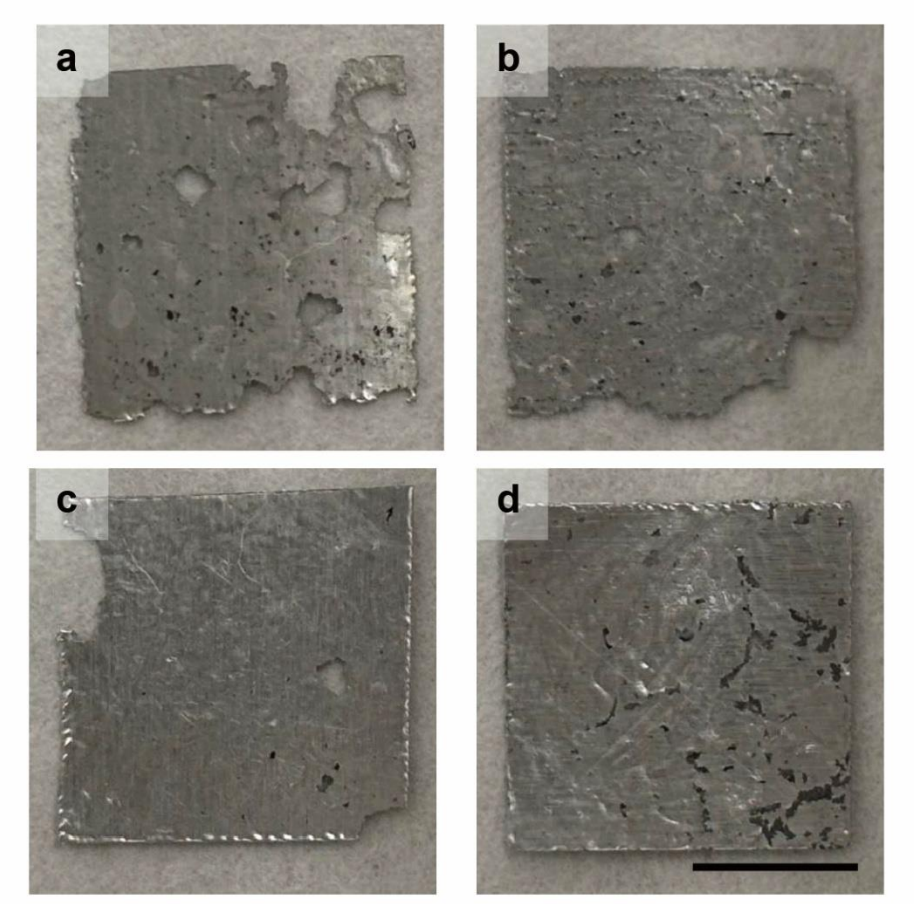

Fig. S7 Optical images of Al anode after 24 h of exposure to **a,** 1 m, **b,** 5 m, **c,** 10 m, and **d,** 15 m HHEs. Scale bar denotes 0.5 cm. The optical images of the Al foils after 24 h of contact with HHEs reveal a clear concentration-dependent difference in self-corrosion behavior. The Al foil exposed to the 1 m HHE showed the most severe surface degradation and mass loss, indicating substantial parasitic corrosion under dilute electrolyte conditions. As the LiCl concentration increased from 5 m to 15 m, the extent of visible surface damage progressively decreased, suggesting that the self-corrosion of Al was effectively suppressed in the more concentrated HHEs. These observations visually support the improved anticorrosion capability of concentrated HHEs and explain the enhanced anode utilization and discharge performance of the corresponding H-AABs.

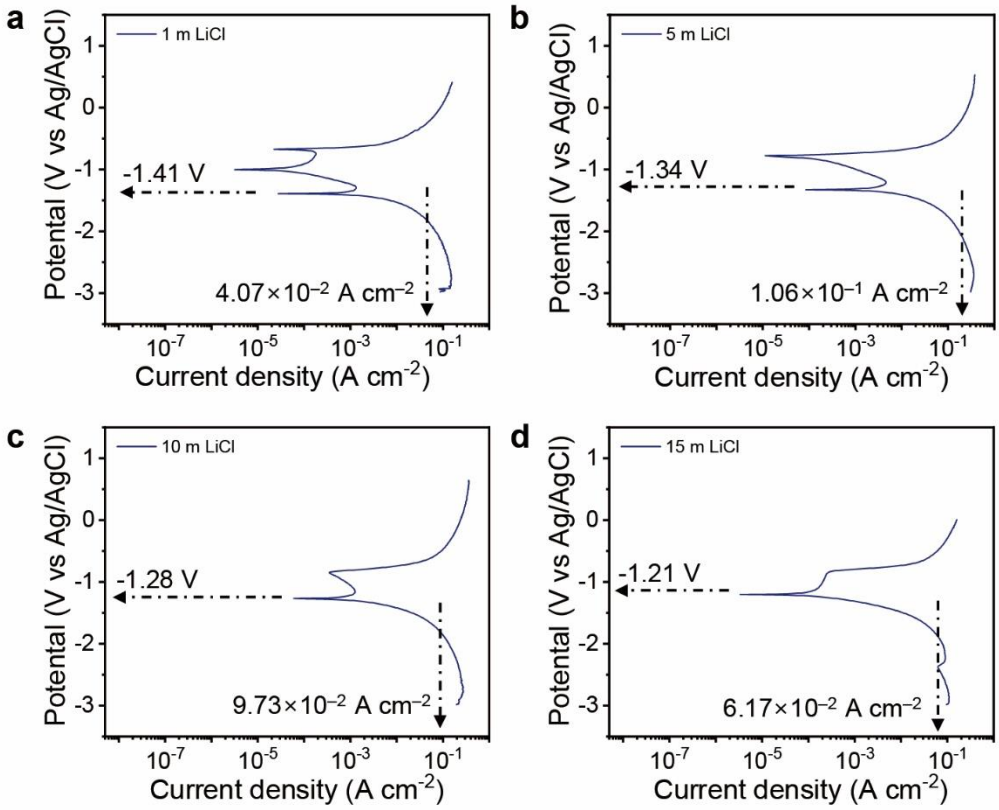

Fig. S8 Tafel plots of Al anode in **a,** 1 m, **b,** 5 m, **c,** 10 m, and **d,** 15 m LiCl solutions at a scan rate of 10 mV s^{-1}. Tafel polarization analysis further revealed that the corrosion behavior of the Al anode strongly depended on the LiCl concentration of the HHEs. As the concentration increased, both the corrosion potential (E_{Corr}) shifted toward more positive values from –1.41 to –1.21 V, indicating an increasingly stabilized electrochemical environment for the Al surface. In addition, the corrosion current density (j_{Corr}) decreased from 0.1 to 0.06 A cm^{-2} for the 5 and 15 m HHEs, respectively, demonstrating a clear reduction in corrosion kinetics at higher concentration. These results indicate that Al corrosion reactions are both thermodynamically and kinetically suppressed in highly concentrated hygroscopic HHEs, which is consistent with the reduced activity of water molecules in the concentrated electrolyte environment.

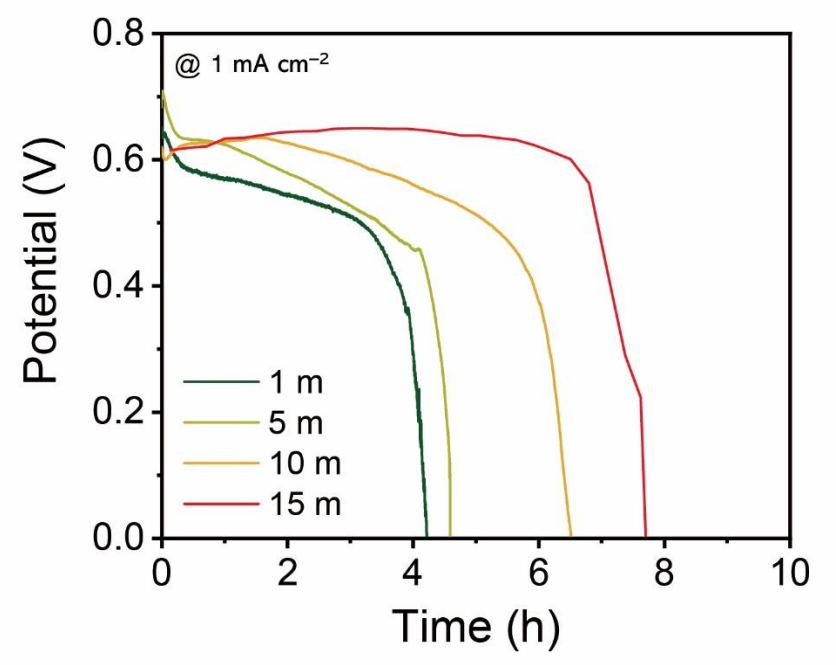

Fig. S9 Discharge profiles of H-AABs using HHEs with different HHE concentration at 1 mA cm^{-2} and 60% RH. Highly concentrated HHEs enabled higher discharge potential and specific capacity, which can be attributed to their stronger hygroscopicity that allows more effective water uptake and retention required for sustained battery operation, as well as their ability to suppress parasitic Al corrosion.

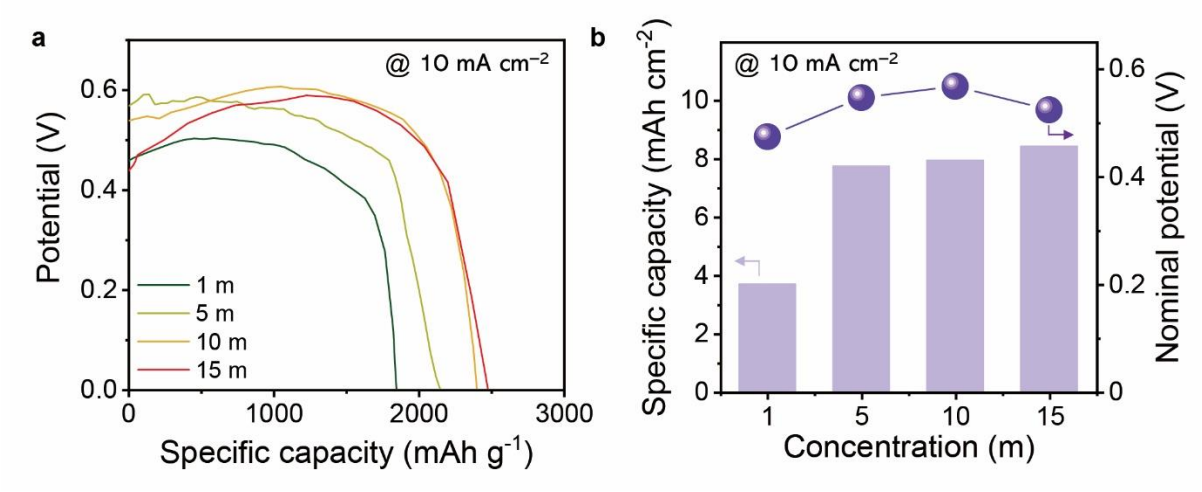

Fig. S10 a, Discharge profiles of H-AABs utilizing various concentration of HHEs at 10 mA cm^{-2} and 60% RH. **b,** Concentration-dependent specific discharge capacity and nominal potential of the H-AABs under air at 60% RH and 10 mA cm^{-2}. The improved discharge capacity at high current density can be attributed to two synergistic effects in the highly concentrated HHEs: stronger hygroscopicity-driven water uptake/retention for sustained ORR and reduced Al self-corrosion through suppressed water activity. Among the tested concentrations, the 15 m HHE showed the highest discharge capacity and was therefore selected as the optimized composition. Although further increasing the LiCl concentration could potentially enhance hygroscopicity and corrosion suppression, concentrations above 15 m introduced processing limitations. In experiments up to 19 m LiCl, AAm, MBAA, and KPS were not fully dissolved in the precursor solution, preventing the formation of homogeneous HHEs. This behavior is likely associated with reduced water activity near the LiCl solubility limit, which restricts precursor dissolution and compromises gel uniformity. Therefore, the 15 m HHE was chosen as the highest processable concentration that balances electrochemical performance, water management, corrosion suppression, and hydrogel uniformity.

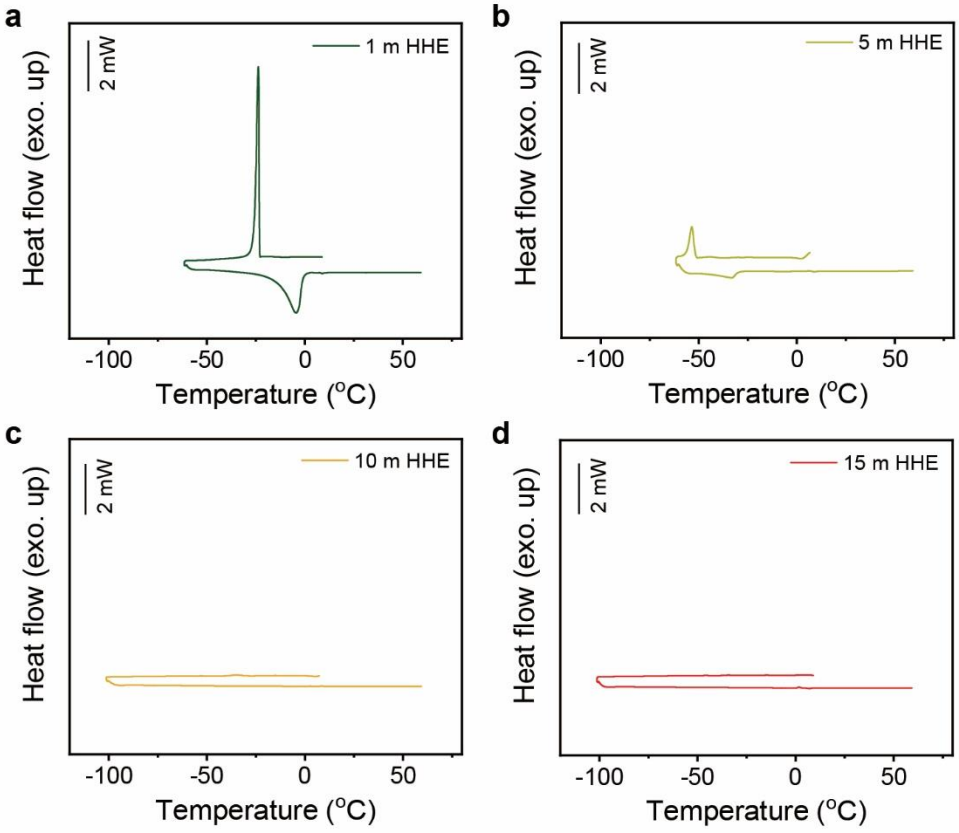

Fig. S11 DSC cycles of **a,** 1 m, **b,** 5 m, **c,** 10 m, and **d,** 15 m HHEs. Heating and cooling rate is 5 °C min^{-1}. Thermal and spectroscopic analyses revealed the physicochemical environment of water molecules in the HHEs. At 1 m, a melting point was observed at 0 °C and a crystallization peak appeared at –23.3 °C. However, as the concentration increased, the phase-transition temperature shifted to lower values, while the enthalpy of crystallization decreased and disappeared completely above 10 m. At low concentration, the distinct phase-transition features suggest the presence of free water molecules. In contrast, as the concentration increases, these transition behaviors disappear, indicating that water molecules are confined within ion–water–polymer interaction networks. Such confinement suppresses molecular rearrangement of water and thus inhibits ice-crystal formation, reflecting the reduced water activity in highly concentrated HHEs

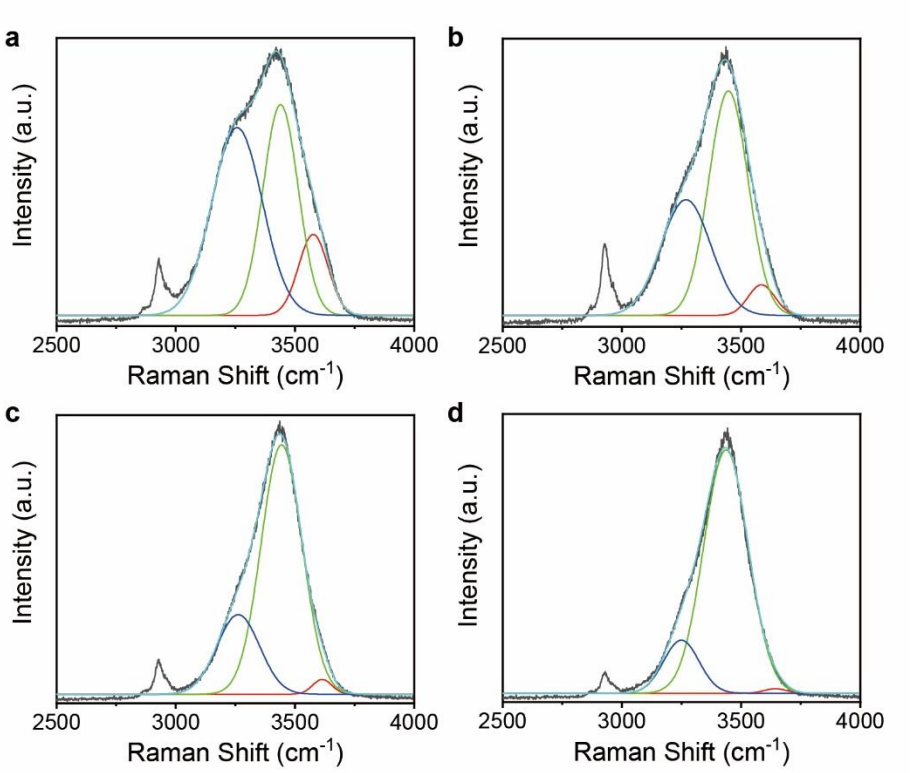

Fig. S12 Deconvoluted Raman spectra of **a,** 1 m, **b,** 5 m, **c,** 10 m, and **d,** 15 m HHEs in the range of 3,000 to 4,000 cm^{-1}. With increasing concentration from 1 to 15 m, the free νOH_{free} (3,580 cm^{-1}) and νOH_{Sym} (3,262 cm^{-1}) continuously decreased, whereas the νOH_{Asym} (3,441 cm^{-1}) became dominant. The fraction of free water molecules was reduced to 0.8% in the 15 m HHEs, while the asymmetric –OH component increased to 84.5%. This pronounced spectral change indicates that the intermolecular H-bond network among water molecules is progressively weakened as the number of available water molecules decreases. Instead, water molecules are more strongly engaged in asymmetric coordination environments associated with ion solvation and hydrogen bonding to the polymer–ion matrix. Therefore, the highly concentrated HHEs contain far less bulk-like free water and a much larger fraction of ion-associated water.

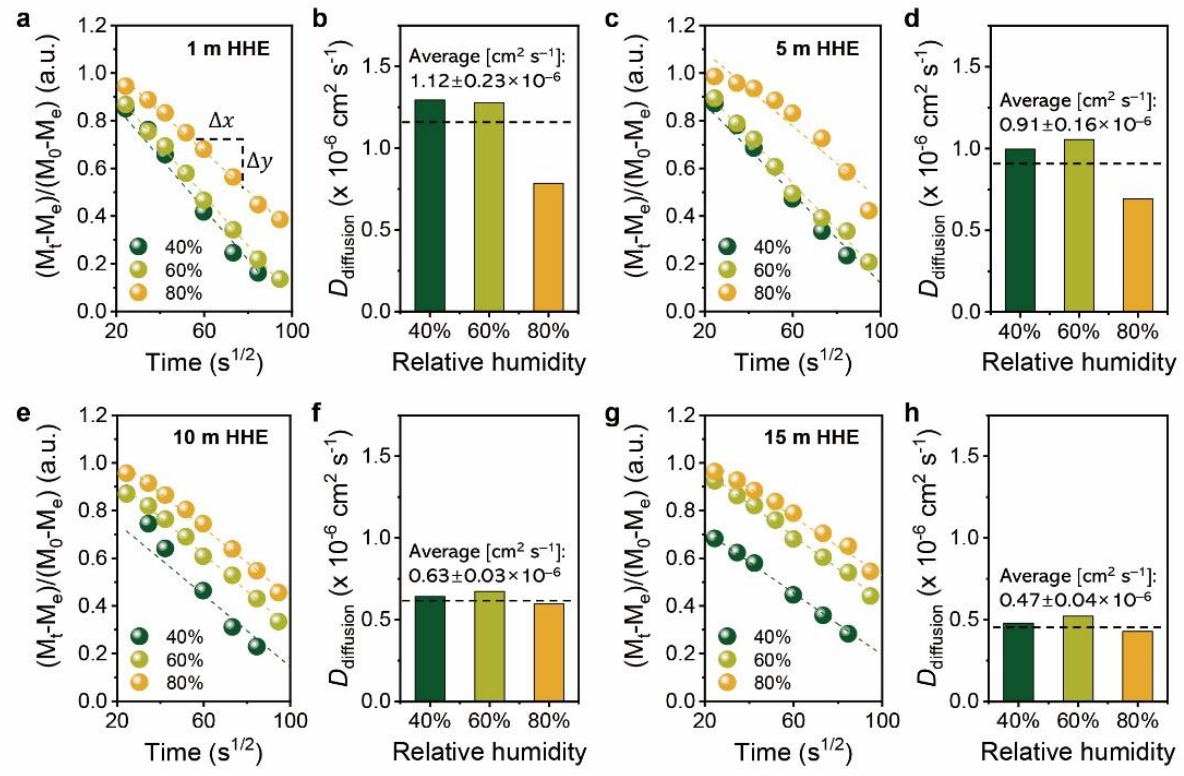

Fig. S13 RH-dependent diffusion model of water molecules, with linear fitting shown as dashed lines in **a,** 1 m **c,** 5 m, **e,** 10 m, and **g,** 15 m HHEs. Diffusion coefficients calculated from the slopes of the linear fits in **b,** 1 m **d,** 5 m, **f,** 10 m, and **h,** 15 m HHEs. Although the extent of water uptake increased under more humid conditions, the calculated $D_{diffusion}$ remained unchanged over the tested concentration range of HHEs. The average $D_{diffusion}$ gradually decreased from 1.12, 0.91, 0.63 and 0.47 × 10^{-6} cm^2 s^{-1} as the HHE concentration increased from 1 to 15 m. This behavior indicates that water transport in the HHE is not dictated by the external humidity itself, but rather by the internal physicochemical environment including porosity, tortuosity, and ion-polymer interaction of the HHEs.

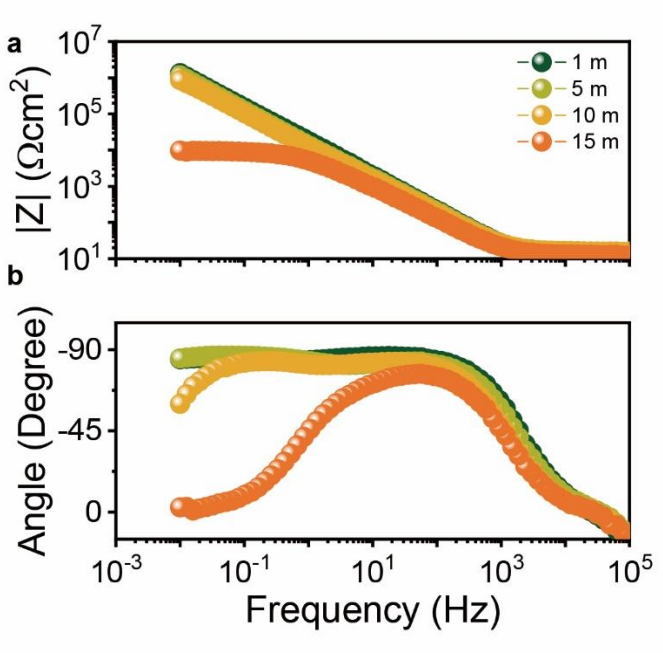

Fig. S14 a, Bode impedance plots and **b,** Bode phase plots of various HHEs. Although diffusive transport becomes more restricted at higher HHE concentrations, the discharge performance of the H-AABs is improved rather than degraded. This finding suggests that, in ultrathin HHE systems, stabilization of the local chemical environment through reduced water activity and suppressed parasitic corrosion is more important than maximizing molecular diffusional mobility.

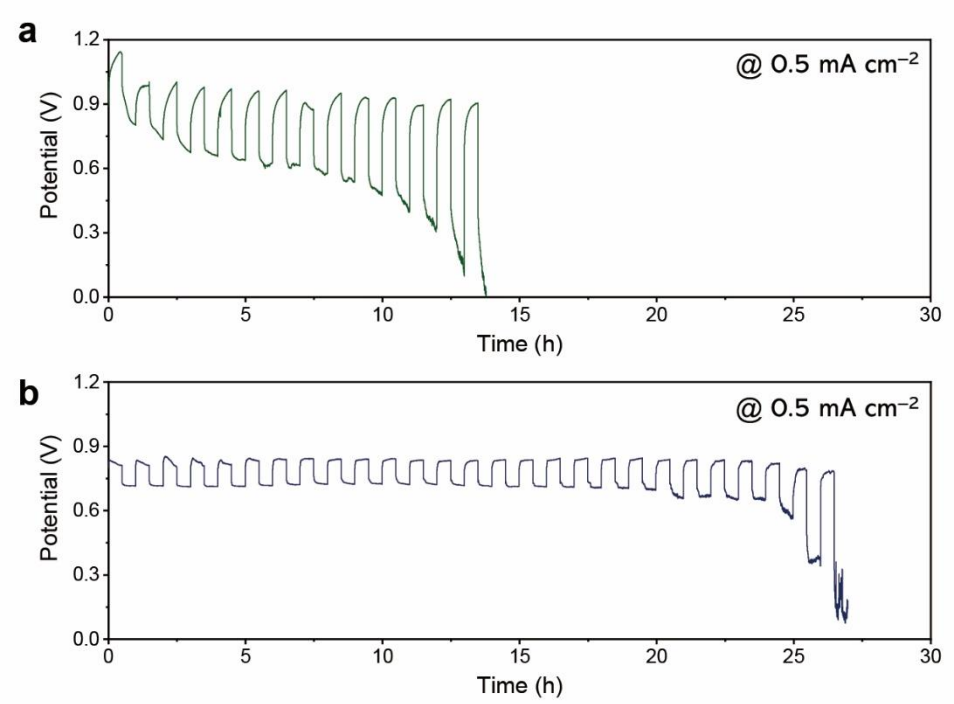

Fig. S15 On−off cycling of **a,** 1 m and **b,** 15 m H-AABs at 0.5 mA cm^{-2}. Each on/off duration is 30 min. The cycling performance of the 1 m H-AABs was limited to 14 h, corresponding to a discharge capacity of 3.45 mAh cm^{-2}. During the rest periods, when no useful discharge reaction occurred, the Al anode was still exposed to the electrolyte and thus underwent only parasitic self-corrosion, leading to substantial capacity loss. In addition, dehydration of the gel electrolyte further limited the long-term operation of the low-concentration HHEs. In contrast, the 15 m H-AABs exhibited markedly improved performance because the concentrated electrolyte effectively suppressed Al self-corrosion and stabilized the anode. Moreover, the hygroscopic nature of the 15 m HHE helped retain water, thereby maintaining ion transport and extending the on/off cycling duration to approximately 27 h, corresponding to a discharge capacity of 6.75 mAh cm^{-2}, and demonstrating improved long-term operational stability.

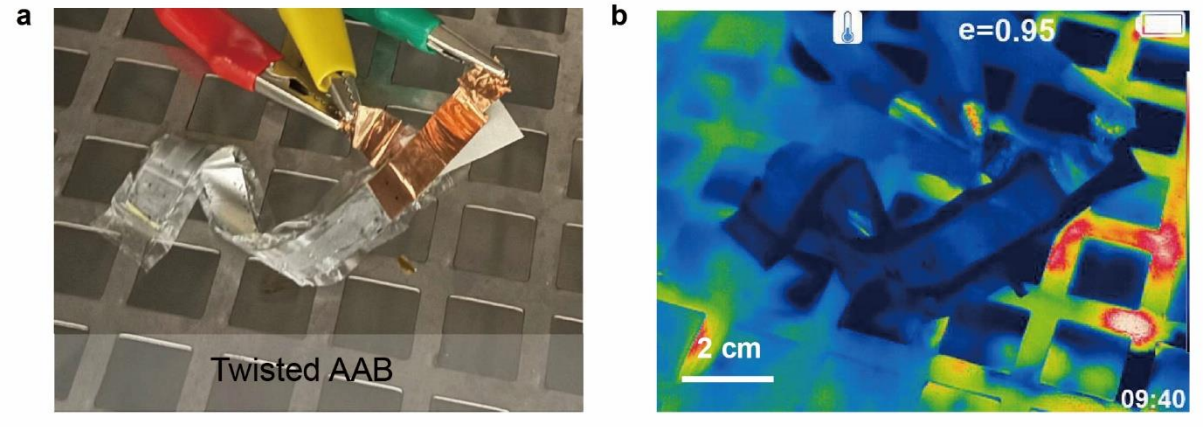

Fig. S16 a, Real and **b,** thermographic photos during galvanostatic discharge at 1 mA cm^{-2}. The thermographic images suggest that the hydrogel-based H-AAB can effectively moderate heat generated during discharge, thereby preventing noticeable local hot spots on the cell surface. Such thermal-buffering behavior is especially beneficial for on-skin applications, as it helps maintain a skin-compatible operating condition despite the exothermic nature of Al oxidation.

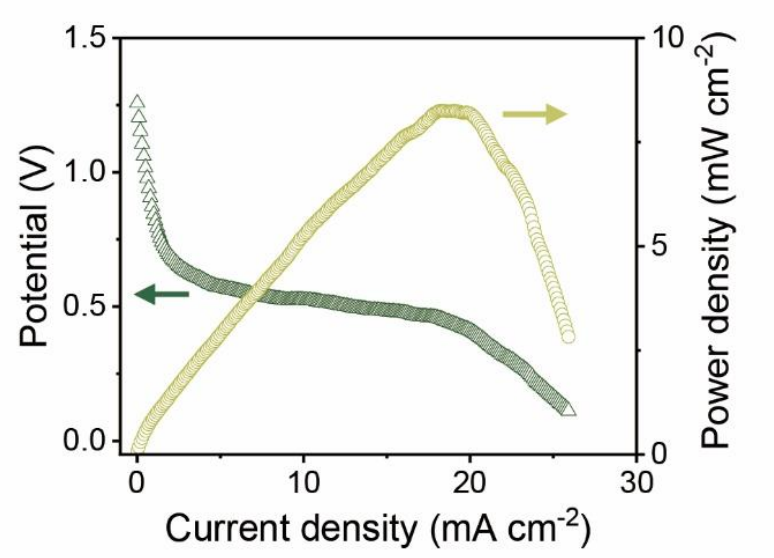

Fig. S17 Galvanodynamic analysis and power density of the H-AABs. The H-AABs exhibited a maximum power density of 8.3 mW cm^{-2} at 20 mA cm^{-2}, demonstrating their practical power-delivery capability for wearable and epidermal electronics. Notably, as the current density increased, the discharge voltage was relatively well maintained over the range of approximately 3–15 mA cm^{-2}, indicating stable operation under moderate current loads. The power density increased continuously with increasing current density up to 20 mA cm^{-2}, where the maximum value was reached, and then decreased sharply at higher current densities.

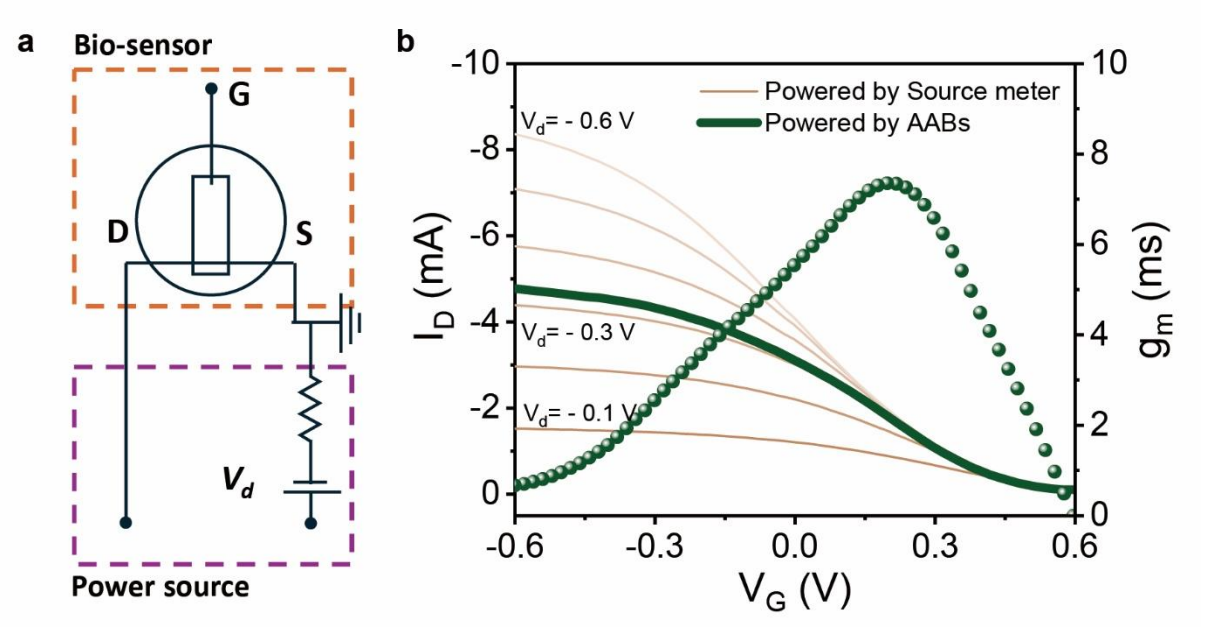

Fig. S18 a, Equivalent circuits of organic electrochemical transistor (OECT)-based biosensor systems for EMG measurements. **b,** Transfer curves of the OECT-based biosensor powered by a source-meter and H-AABs. The equivalent-circuit model supports the validity of the OECT-based biosensor configuration for EMG measurements. In addition, the transfer curve obtained with the H-AAB was comparable to that measured under a 0.3 V bias from a source meter, with a transconductance of approximately 8 mS, indicating that the battery can stably operate the transistor-based biosensor rather than merely supplying a voltage.

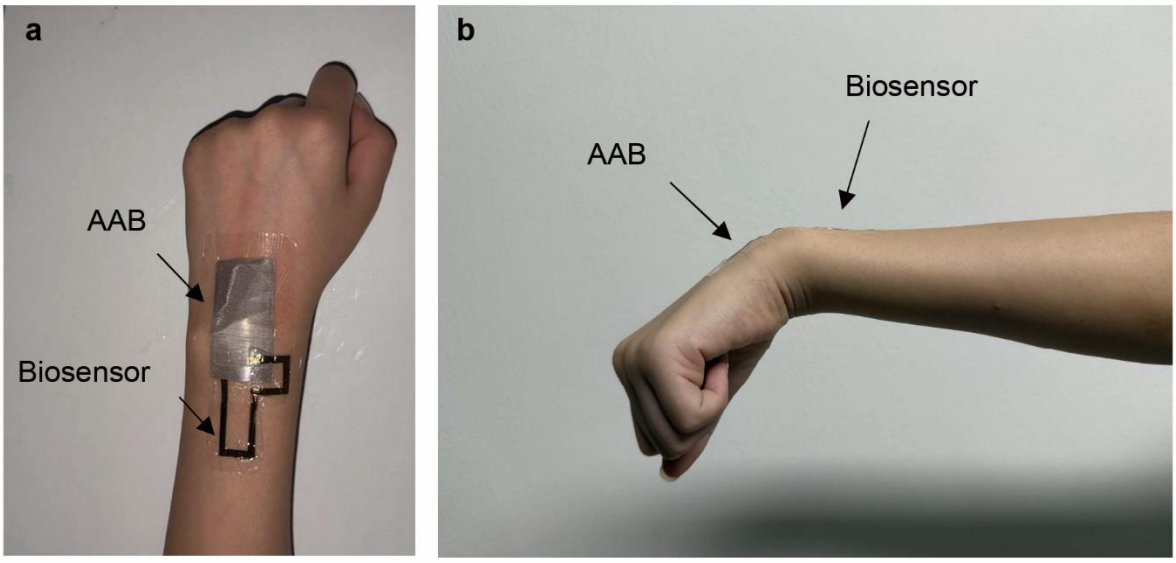

Fig. S19 a, Top view and **b,** side view of the integrated skin-conformal EMG sensor system. The integrated EMG sensor system was conformally attached to the skin surface. Owing to its ultrathin form factor, the device was barely visible in the side view.

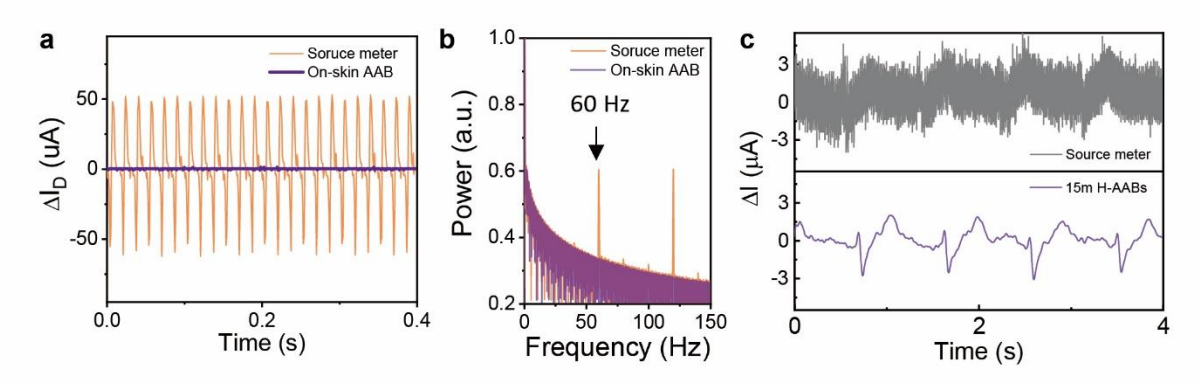

Fig. S20 a, Drain current of the biosensor with a bias applied by a source meter and on-skin AABs. **b,** Amplitude spectra as a function of frequency, obtained by fast Fourier transform analysis. **c,** ECG signals of OECT-based biosensors powered by a source meter and 15 m H-AAB. The substantially reduced noise under H-AAB powering demonstrates a system-level advantage of the integrated on-skin design. Eliminating bulky external biasing equipment and shortening the electrical connection between the power source and biosensor suppress environmental interference, thereby improving the clarity and fidelity of the recorded ECG signals.

Supplementary Tables

Table S1. Time-dependent ionic conductivity of the HHEs under the air at 60% RH.

Time (h)	Ionic conductivity (mS cm^{-1})			
	1 m	5 m	10 m	15 m
0	6.05	7.83	8.35	2.45
1	5.83	7.97	8.79	2.44
2	5.68	7.97	8.79	2.45
3	5.54	7.97	8.72	2.46
4	5.40	7.97	8.79	2.48
5	5.31	8.05	8.79	2.47

Table S2. Concentration-dependent corrosion potential and current density of Al anode. These data were extracted from Tafel plots in **Supplementary Fig. S8**.

LiCl	E_{corr}	E_{pass}	E_{water}	J_{corr}	J_{pass}	J_{water}
[m]	[V vs Ag/AgCl]			[A cm^{-2}]		
1	-1.41	-1.01	-0.68	4.70×10^{-2}	5.64×10^{-5}	2.14×10^{-4}
5	-1.34	-0.79	–	1.06×10^{-1}	1.82×10^{-4}	–
10	-1.28	-0.86	–	9.73×10^{-2}	4.70×10^{-4}	–
15	-1.21	-0.81	–	6.17×10^{-2}	2.77×10^{-4}	–
H_2O	–	–	-0.58	–	–	1.41×10^{-6}

Table S3. Ratio of the number of water molecules to ions in different LiCl concentrations.

Concentration (m)	LiCl (g)	Water (g)	Water to ions ratio (mol mol^{-1})
1	0.28	6.65	27.8
5	1.41		5.6
10	2.82		2.8
15	4.23		1.8